Epitaxial Polysilicon MEMS Temperature Sensor with 0.043 ℃ Resolution at 4-Hz Data Rate

Paolo Frigerio, Andrea Fagnani, Valentina Zega, *Member, IEEE*, Gabriele Gattere, and
Giacomo Langfelder, *Member, IEEE*

Abstract— **This work discloses a temperature sensor based on a polysilicon MEMS resonator. The system exploits the temperature drift of the resonance frequency of two modes of a single MEMS structure, and associated analog and digital electronics. The temperature coefficient of the two modes is found to differ by about 2 ppm/℃, enough to enable the implementation of a relative counting technique to measure the relative temperature. The design uses phase-locked loops to compensate for the challenge posed by the similarity between resonance frequencies and temperature coefficients of the two modes, which otherwise would hinder the achievable resolution. The temperature readout is entirely digital, based on counters and a combinational logic that computes temperature in real-time. The sensor achieves 0.043 ℃ resolution with a 4 Hz output data rate. Fabricated in epitaxial polysilicon, this implementation is compatible with on-chip temperature measurement of large-volume, polysilicon-based inertial sensors, as a substitute for (or additional aid of) on-board or on-ASIC temperature sensors. The latter may be affected by spatial and temporal temperature differences with respect to the MEMS substrate, as extensively proved in this work.**
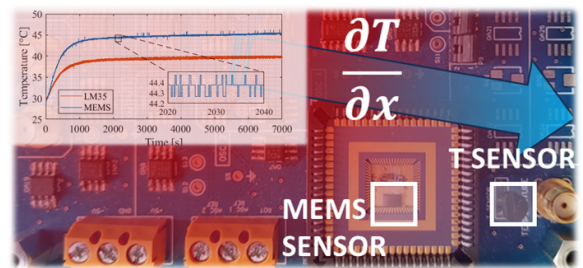
Index Terms— **MEMS, polysilicon, resonators, temperature sensor.**

I. INTRODUCTION

THE operation of any electronic transducers depends, among other things, on robustness to temperature variations. Indeed, devices are designed to work in environments where temperature can vary on a wide range, defined according to the specific application. In addition, the actual operating temperature depends not only on the external environment, but also on the transducer material, assembly and surrounding electronic components, including their thermal transients.

Knowledge of the true operating temperature is of the utmost importance. This is especially challenging for systems where the temperature estimate cannot be implemented directly on the transducer die. Most microelectromechanical systems (MEMS) fall within this scenario, and stability is becoming the limiting factor for high-end applications [1].

Over the years, many techniques to mitigate temperature effects have been studied and implemented. For example, in the area of MEMS, a first methodology involves compensation at process level: combination of different materials [2], [3] or combined doping concentrations and crystallographic directions [4]–[8] have shown to improve the stability of time

Submitted for review on XXX.
Paolo Frigerio (e-mail: paolo.frigerio@polimi.it), Andrea Fagnani (e-mail: andrea.fagnani@polimi.it), Valentina Zega (e-mail: valentina.zega@polimi.it), and Giacomo Langfelder (e-mail: giacomo.langfelder@polimi.it) are with Politecnico di Milano, Italy.
Gabriele Gattere (e-mail: gabriele.gattere@st.com) is with STMicroelectronics, Cornaredo, Italy.

references. Here one disadvantage is the increased production cost, due to an increased number of process steps.

Therefore, an electronic calibration and subsequent compensation is often used, which involves the introduction of a temperature (T) sensor and dedicated circuitry [9]. The most common solution is to use a T sensor in the application specific integrated circuit (ASIC) associated with the MEMS device. Alternatively, when the system relies on discrete components, a stand-alone T sensor is mounted on the board. The sensor implementation in both cases usually exploits bipolar juction transistors (BJT) [10]: by exploiting the dependence of the base-emitter voltage on temperature and using two devices with different dimension and bias current, it is possible to generate an output voltage proportional to absolute temperature (PTAT). The sensor is however positioned few mm to few cm away from the transducer, separated by a non-null thermal resistance (glue, board layers, package, air...).

The use of MEMS technology for direct temperature measurement has been recently given increasing attention. This is due to the possibility to integrate the T sensor on the same die of other MEMS transducers, so as to increase precision and accuracy. Indeed, the main advantage is that the distance between the MEMS (whose temperature has to be measured) and the T sensor is reduced and they both lie on the same silicon substrate thus nulling the thermal resistance in between. Therefore, temperature estimation errors induced by heat gradients, whether spatial or temporal, are minimized.

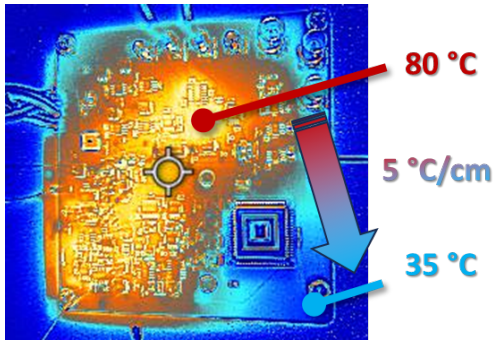A first example was reported in [11], where the struc-

Fig. 1. Example of a significant temperature gradient across a MEMS gyroscope board measured with a thermal camera. The heat source is a variable-gain amplifier located far from the gyroscope, which is housed within the ceramic carrier in the bottom-right corner.

tural resistance of a MEMS element, highly dependent on temperature, was used for the estimation. Another solution, based on a dual-MEMS resonator, was proposed in [12]. Here, temperature is extracted from the ratio of two 50-MHz-range resonance frequencies, which have largely different temperature coefficients o f f requency (TCf), enabling a 20 µK resolution. To achieve this performance, once again combined doping concentrations and different crystallographic directions are needed in a monocrystalline silicon process. The use of different TCfs in a dual-MEMS approach was exploited also in [13], where the combination of a silicon-glass assembly and different lengths of two double-ended tuning fork (DETF) resonators allowed achieving, by their frequency ratio, few 10 mK resolution normalized to 1 Hz bandwidth. An alternative approach based on two MHz-range SiO_2-coated Si DETFs was reported in [14], reaching around 10 mK resolution. Instead of a dual-MEMS approach, a multi-mode approach, where different vibrating modes of the same structure show different TCfs, was exploited in [15]. Another approach was presented in [16], relying on the TCf difference between the Lamè mode and the square-extensional mode in a silicon resonator. Using relatively large – but similar – modal frequencies (12 MHz and 13 MHz), the authors were able to achieve sub 10 mK resolution.

Several large-volume, consumer-grade, MEMS processes are however based on polysilicon instead of monocrystalline silicon, and a strategy to locally sense MEMS temperature in this situation would be beneficial. I n a p revious w ork [17], the possibility to obtain a TCf difference between two modes (flexural a nd t orsional) o f t he s ame l ow-doped polysilicon MEMS resonator was demonstrated. This approach benefits from the repeatability of the TCfs from part-to-part, resulting from the relatively low doping concentration. However, the temperature resolution is poor because of the small TCf difference and small frequency ratio between modes. A solution to this issue is to artificially increase the difference between the two eigenfrequencies through a phase-locked-loop (PLL), so as to improve resolution without sacrificing the output data rate (ODR). The approach was preliminarily introduced in [18].

This paper completes the research by combining a dual-mode resonator with self-sustaining circuits, PLLs to increase the frequency ratio, and an FPGA-based digital temperature

calculator, which outputs the temperature data. Additionally, noise and calibration procedures are discussed in detail. The system is tested in different scenarios to validate its performance, also against an on-board reference T sensor.

The manuscript is structured as follows: Section II introduces the specification r equirements, c onsidering a practical case study related to high-end inertial sensors. Section III describes the resonator and the system implemented for temperature readout. Section IV describes the sensor calibration. Section V shows the result of experimental validation. Finally, Section VI concludes the paper.

II. APPLICATION REQUIREMENTS

The target application for the proposed sensor is temperature measurement within the same silicon die of another MEMS sensor, e.g. an accelerometer or a gyroscope, implemented using the same polysilicon process. The resolution demanded to the T sensor is dependent, in turn, on the temperature stability requirement of the application sensor: this Section, therefore, analyzes a case study to extract the T sensor specifications.

Consider a MEMS accelerometer with a typical uncompensated ZGO (zero-g offset) drift of about 1 mg/°C (see e.g. [19]), working in a range between −40 °C and 125 °C. Assume that, after compensation, the target stability across the above range needs to be 50 µg, as required by high-end applications [20]. In order to perform a proper compensation, the resolution demanded to the T sensor in turn becomes 0.05 °C.

If the on-board or in-ASIC T sensor is located far from the MEMS sensor, then there may be a significant difference between the temperature experienced by the two devices. In particular, high-end inertial sensing applications require low noise, large bandwidth and large dynamic range, leading to increased power consumption. Such power requirements bring increased heat dissipation and high temperatures. The maximum distance between the sensors to avoid unacceptable errors in the T measurement depends thus on the heat distribution in the system. An example is drawn from a reference scenario, represented by the thermal image of a board hosting a MEMS gyroscope and its associated board-level circuitry, shown in Fig. 1. It should be noted that the circuitry used to operate the gyroscope can generate enough heat to locally raise the temperature up to 80 °C, thus creating a 5 °C/cm gradient towards the edges of the board, where a temperature of 35 °C is measured. Even assuming the temperature sensor is mounted as close as possible to the sensor, if the relative distance is 1 cm the error in measuring temperature is 5 °C, 100 times larger than the demanded precision calculated above. Furthermore, even if the temperature sensor is integrated inside the sensing ASIC, and the latter is placed directly on top of the MEMS sensor with a relative distance of 1 mm, the measurement error can still be 0.5 °C, thus obviously hindering compensation of temperature-dependent parameters.

An on-MEMS-chip temperature sensing is a possible solution to bypass not only effects of spatial temperature gradients, but also time-varying heat generation by on/off components switching on the board/ASIC.
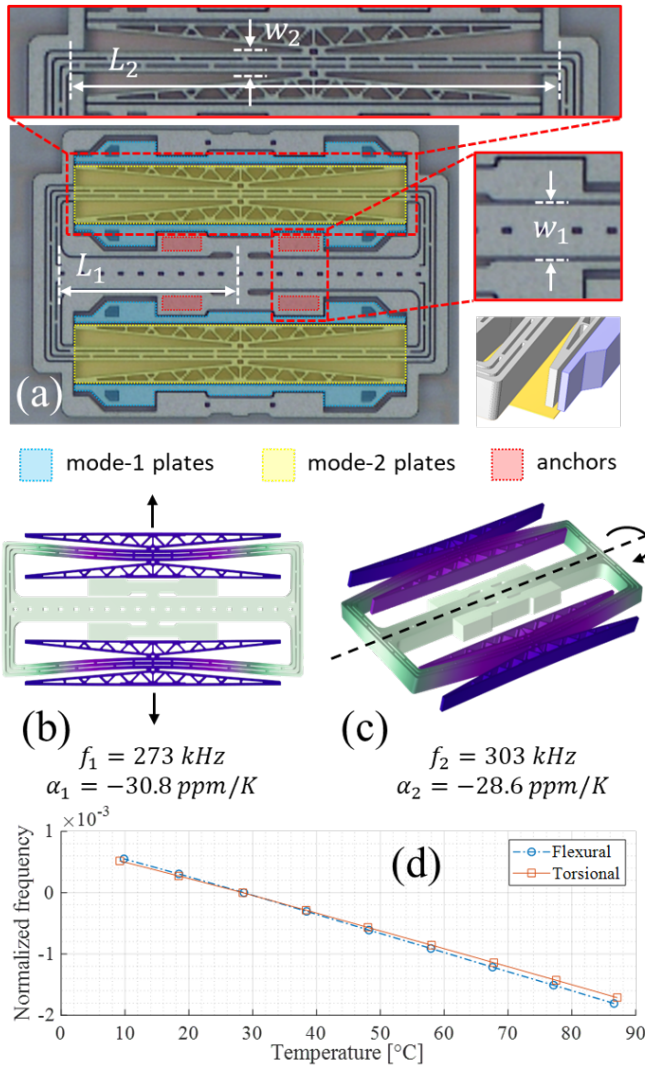
Fig. 2. Scanning-electron microscope picture of the MEMS resonator (a), where the electrodes used for actuating the two modes are high-lighted. The position of the out-of-plane electrodes below the structure is illustrated in the zoomed 3D model. The mode shapes are shown in (b) and (c), with the corresponding frequencies and temperature coefficients. The measured resonance frequency vs temperature is shown in (d) for both modes, normalized to the value at room temperature.

TABLE I
DESIGN PARAMETERS OF THE MEMS RESONATOR.

Mode	f_0 [kHz]	R_m [MΩ]	C_m [aF]	L_m [kH]
1	273.03	0.78	147.2	2.3
2	303.92	0.19	291.7	0.94

MEMS inertial sensor, to avoid a relevant increase in the die size; second, the sensor shall be optimized in order to obtain the largest possible difference in the temperature coefficients of the modes. According to the procedure presented in [8], a custom Finite Element model has been developed to estimate the TCfs, considering the temperature dependencies of material constants, extrapolated from the literature. Uncertainty in such dependencies, especially for the adopted low-doped polysilicon, yields some quantitative discrepancies between estimate and measurement. In particular, there is an offset between the estimated and measured values, but the difference is well matched by experimental data. Such design results in about 2 ppm/°C difference between the linear coefficients of the two modes, both in the order of −30 ppm/°C [17]. The normalized frequency vs temperature curves, measured in the preliminary characterization campaign and used to calculate the temperature coefficients, are shown for both modes in Fig. 2d.

Both modes of the suspended structure, biased at around 20 V, are actuated and sensed by parallel-plate capacitive electrodes (see zoom in Fig. 2a), whose bias voltage is 0 V.

Each mode can be modeled by an equivalent admittance in the Laplace domain:

$$\frac{i_m(s)}{V_a(s)} = \frac{1}{L_m s + R_m + \frac{1}{sC_m}} \tag{1}$$

where V_a is the voltage applied to the actuating electrodes, i_m is the motional current induced by the structure displacement on the sensing electrodes, and R_m, C_m, L_m are an equivalent resistance, capacitance and inductance. Their values for the two modes of the resonator are listed in Table I.

The devices are manufactured by STMicroelectronics through a fabrication technology capable of delivering large-volume inertial sensors. Given the relatively low doping value of polysilicon, this process allows to obtain resonators which, for a given mode, show a very repeatable TCf from part to part [17]. The resonators are encapsulated by glassfrit bonding with getter, resulting in a 0.7 mbar nominal cavity pressure. In order to reduce the impact of package stress on the resonator, the devices are bonded to a ceramic carrier with a low-stress adhesive tape. The carrier is hosted within a socket that is directly soldered on the board with the electronic circuitry.

III. System Implementation

A. MEMS Resonators

The 24 μm thick MEMS resonator is shown in Fig. 2a. It is formed by a scissor-jack structure, with $w_1 = 31.1$ μm wide and $L_1 = 170.6$ μm long inner beams, ending on the central anchor point to the substrate, and $w_2 = 14$ μm wide and $L_2 = 341.2$ μm long outer beams. Slots are inserted within the beams width to minimize thermoelastic damping [21]. The flexural and torsional modes are represented in Fig. 2b and Fig. 2c, respectively. The flexural mode will be referred to as "mode 1" in the following, while the torsional mode will be referred to as "mode 2". These modes show a slightly different drift of the resonance frequency with temperature, due to the difference in the modal stiffness and weight of the Young and shear moduli. The device design considers two aspects: first, the area should be smaller than the typical

B. Analog Electronics

A printed-circuit board (PCB) was designed with the circuitry to maintain two modes in simultaneous stable oscillation. The MEMS is hosted directly on the PCB with the electronic circuit, so to minimize parasitic effects between the MEMS and the front-end.
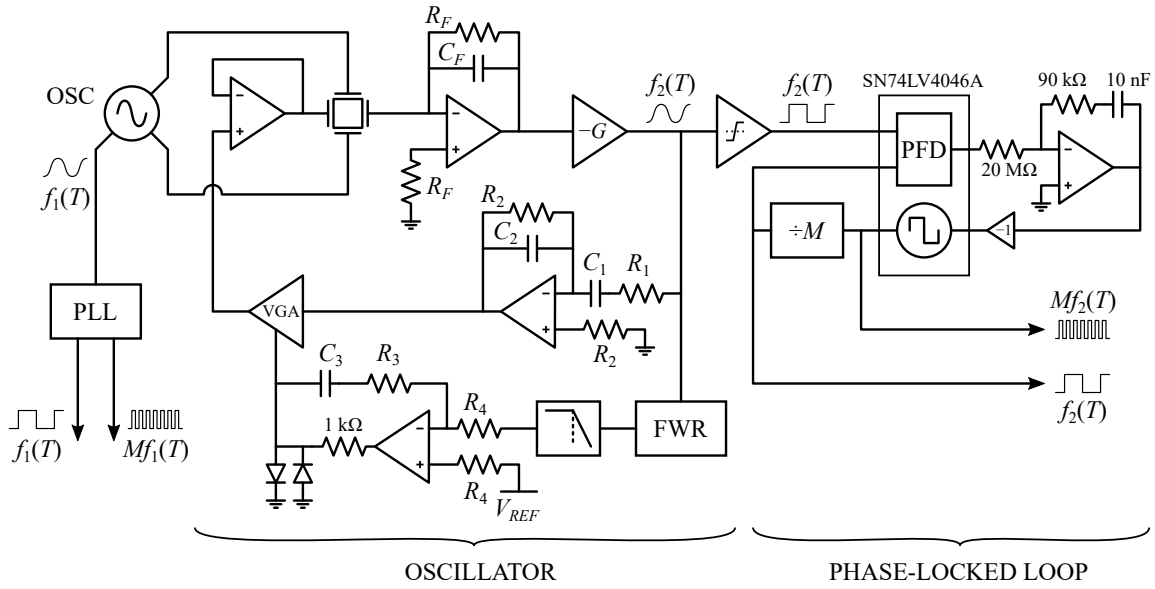
Fig. 3. Schematic of the analog circuitry, including the oscillators and the PLLs, shown in detail for mode n. 2 and only schematically (left of the figure) for mode n. 1. The signals used for the temperature estimate are $f_1(T)$ and $Mf_2(T)$. Provided here is a list of the main component values: $C_F = 4\text{pF-8pF}$, $R_F = 100\,\text{M}\Omega$, $R_1 = 5\,\text{k}\Omega$, $R_2 = 500\,\text{k}\Omega$, $C_1 = 15\,\text{nF}$, $C_2 = 200\,\text{pF}$, $R_3 \approx 500\,\text{k}\Omega$, $R_4 \approx 100\,\text{k}\Omega$, $C_3 = 10\,\text{nF}$.

The two modes oscillate simultaneously thanks to two identical fully-analog circuits. Fig. 3 reports their detailed schematic for one mode only (the other mode is only schematized for the sake of completeness).

The front-end implemented to readout the motional current of each of the two modes is a charge amplifier, followed by an inverting gain G. Due to the different transduction value of the capacitive ports of the torsional and translational modes, the feedback capacitances are set to different values (4 pF and 8 pF, respectively), so to match the full voltage swing at the output of the gain stage. This optimizes phase noise performance. The feedback resistance of the amplifiers is set to 100 MΩ so that the pole falls well before resonance, and the resistor current noise becomes negligible. The control architecture consists of a $+90°$ phase-shifter followed by a variable-gain amplifier (VGA). The first guarantees to match Barkhausen criteria of oscillation, and is implemented through a negative integrator with a zero in the origin and two poles well before resonance (values of passive components are given in the figure caption). The second, whose gain is controlled by an amplitude regulator circuit, maintains the maximum displacement within a boundary set by an external reference voltage V_{REF}. The regulator maintains the amplitude of the output of the front-end amplifier within few hundreds of mV. This limits the maximum displacement of the beams to less than 5% of the gap between the mass and the fixed electrodes, thus limiting electrostatic non-linear effects. The PCB with the oscillators is shown in Fig. 4a.

The oscillation frequency is then measured by a square-wave derived from the front-end output. As detailed in the next section, the technique used for temperature readout introduces a quantization error that can be improved by increasing the ratio between the mode frequencies. Since the native ratio is close to one, a phase-locked loop (PLL) circuit has been
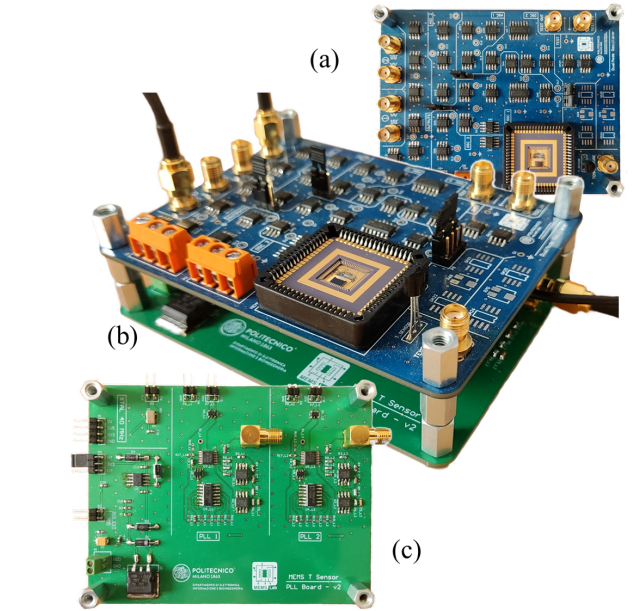

Fig. 4. Picture of the PCB stack (b) hosting the analog circuitry. The oscillator and MEMS are hosted on the top board (a), while the two PLLs are implemented on the bottom board (c).

used to increase the native frequency value by a factor M, without changing the temperature dependence. Only one frequency needs increasing; however, to maintain symmetry, one PLL was implemented for each mode. Frequency f_2 is thus effectively multiplied by M, by measuring the output of the voltage-controlled oscillator (VCO). Frequency f_1, instead, is readout at the input of the phase-frequency detector (PFD).

Both PLLs are implemented using off-the-shelf integrated circuits containing a PFD and a VCO and are designed on a separate stacked board, as shown in Fig. 4b-c.

C. Digital Temperature Calculator

Given a reference calibration temperature T_0, the MEMS temperature can be ideally calculated by the frequencies ratio:

$$T = T_0 + \left(\frac{1}{\Delta R(T)} \frac{f_2(T_0)}{f_1(T_0)} (\alpha_2 - \alpha_1) - \alpha_1 \right)^{-1} \qquad (2)$$

where the values of $f_1(T_0)$, $f_2(T_0)$ are derived for each sample from an initial calibration at T_0, α_1 and α_2 are derived from a family calibration (only a few representative parts) across the whole temperature range, and where the term:

$$\Delta R(T) = \frac{f_2(T)}{f_1(T)} - \frac{f_2(T_0)}{f_1(T_0)} \qquad (3)$$

is a function of $f_1(T)$ and $f_2(T)$ which are measured in real-time. The expression can be linearized, resulting in:

$$T = T_0 + \left(\frac{f_2(T)}{f_1(T)} \frac{f_1(T_0)}{f_2(T_0)} - 1 \right) \frac{1}{\alpha_2 - \alpha_1} \qquad (4)$$

This is however acceptable only for small temperature variations from T_0. The linearization error is:

$$\varepsilon_T = -\frac{\alpha_1 \Delta T^2}{1 + \alpha_1 \Delta T} \qquad (5)$$

which becomes as large as 0.13 °C at −40 °C considering that α_1 is approximately −30 ppm/°C. The full nonlinear expression in (2) need thus to be implemented, and is practically performed by the digital counting circuit shown in Fig. 5. One counter is set to measure a fixed number N_1 of cycles of the slowest input frequency f_1. Such a number is determined by the desired output data rate (ODR) of the sensor, and is calculated according to:

$$N_1 = \left\lfloor \frac{f_1(T_{\max})}{\text{ODR}} \right\rfloor \qquad (6)$$

where $T_{\max}$ is the maximum operating temperature of 85 °C, for which the frequency is minimum. This sets a lower bound to the output data rate, which will fluctuate with temperature.

The secondary counter is clocked by the up-scaled frequency $M f_2$. This counter is reset by the end-of-count (EoC) signal of the primary counter. A simple logic with two banks of registers samples the output of both counters each time that the EoC is asserted. Thus the digital circuit outputs the number $N_2(T)$ of cycles of the high frequency that occur within N_1 cycles of the low frequency. A subsequent block, labelled "temperature calculator" in Fig. 5, performs an estimate of the ideal calculation of (2) by implementing the following equation:

$$\widehat{T} = T_0 + \frac{\Delta N_2(T)}{N_1 \dfrac{M f_2(T_0)}{f_1(T_0)} (\alpha_2 - \alpha_1) - \alpha_1 \Delta N_2(T)} \qquad (7)$$

where $\Delta N_2(T) = N_2(T) - N_2(T_0)$. The real temperature T is thus measured, apart from a residual quantization error $q(T)$:

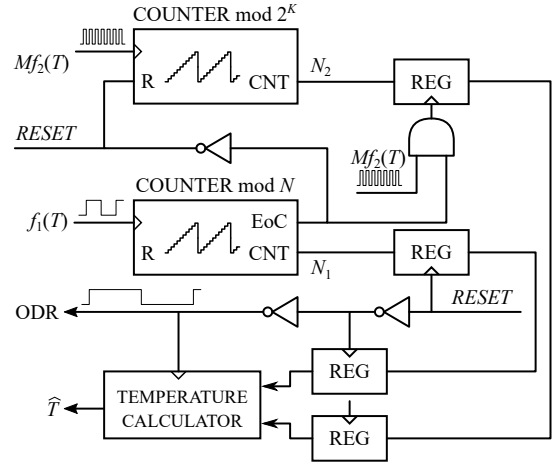$$T = \widehat{T} + q(T). \qquad (8)$$

Fig. 5. Schematic of the digital temperature readout system. A master counter is set to count up to the fixed number N_1, and it manages the reset of the secondary counter. The reset signal also provides a reference for the output-data rate (ODR). The temperature calculator block is a combinational logic that implements equation (7).

The quantization error is due to the truncation of one period of the secondary mode. Thus, it is a function of temperature and it can be approximated by:

$$q(T) \approx q_{\max} \cdot \left(\left\lfloor \frac{\Delta T}{q_{\max}} \right\rfloor - \frac{\Delta T}{q_{\max}} \right) \qquad (9)$$

which is a sawtooth with a maximum quantization error:

$$q_{\max} = \frac{f_1(T_0)}{N_1 M f_2(T_0)(\alpha_2 - \alpha_1)}. \qquad (10)$$

The peak-to-peak quantization error is inversely proportional to the reference number of cycles N_1 and to the clock frequency of the secondary counter. Thus, increasing the secondary mode frequency, i.e., the PLL division modulus, is an additional degree of freedom that can be used to improve the accuracy.

The digital blocks were implemented in an Artix-7 FPGA by Xilinx using fixed-point arithmetic. The calibration parameters T_0, $N_2(T_0)$, $f_1(T_0)$, $M f_2(T_0)$, α_1 and α_2 are stored within dedicated registers. A custom digital interface manages all the digital blocks and enables communication via USB to a host PC. A Matlab routine manages the digital part: load of calibration parameters, enable and reset of the sensor output, and readout of temperature data.

D. System Sizing

As previously shown, the sensor accuracy increases by either increasing N_1 or the PLL division modulus M. Increasing the former means that, since f_1 is fixed, the ODR decreases, and so does the bandwidth. Increasing the latter, however, leads to increased power consumption, complexity and stability issues of the PLL as the VCO frequency increases accordingly. A good compromise is found as follows: assume a target ODR of 4 Hz, which is compatible with temperature variation rates in most applications. In order to achieve a maximum quantization error within ±0.05 °C, for the given ODR the required division modulus needs to be sized at 64, a value compatible with the mentioned PLL constraints.

Mode	T_0 [°C]	$f(T_0)$ [kHz]	α [ppm/°C]	$N(T_0)$
1	25	276.92	-30.85	69079
2	25	296.39	-28.72	4733371

Fig. 6. Schematic view of the digital frequency estimator block used in the initial calibration step. A digital PLL generates the clock reference f_{CK} of 200 MHz for two counters. To reach the desired accuracy in frequency measurement, both input waveforms are scaled by integer factors, both set to 45000.

E. Noise

Since temperature is calculated directly from the frequency, the oscillator phase noise may affect the sensor accuracy. By linearizing (4), and accounting for the PLL, the output power spectral density $S_T(\omega)$ due to the fluctuation of both frequencies can be derived as:

$$S_T(f) = \frac{\dfrac{S_{f1}(f)}{f_{10}^2} + \dfrac{S_{Mf2}(f)}{M^2 f_{20}^2}}{(\alpha_2 - \alpha_1)^2 \left(1 + \dfrac{f^4}{f_{BW}^4}\right)} \tag{11}$$

where $f_{10} = f_1(T_0)$, $f_{20} = f_2(T_0)$, whereas $S_{fi}(f)$ with $i = 1, 2$ is the power spectral density of each mode frequency noise, and $S_{Mf2}(f) = M^2 S_{f2}(f)$. The PLL acts as a low-pass filter on the input frequency, with a closed-loop bandwidth f_{BW} of about 540 Hz. The frequency power spectral density can be described by considering the charge amplifier input-referred voltage white noise S_{vn} as the dominant contribution:

$$S_{fi}(f) = \frac{2S_{vn}\left(1 + \dfrac{C_P}{C_F}\right)^2 f_{i0}^2}{\pi^4 V_{REF}^2}\left(1 + \frac{f_{i0}^2}{4Q_i^2}\frac{1}{f^2}\right)\sin^2\left(\frac{\pi f}{f_{i0}}\right) \tag{12}$$

where C_P is the parasitic capacitance between the negative input of the charge amplifier and ground, Q_i is the mode quality factor. The dominant contribution is the white phase noise component. The expression can be thus simplified, yielding the following equation for the temperature-referred noise standard deviation:

$$\sigma(T) \approx \frac{\left(1 + \dfrac{C_P}{C_F}\right)\dfrac{f_{BW}}{f_{10}}\sqrt{4S_{vn}f_{10}}}{(\alpha_2 - \alpha_1)\pi V_{REF}}. \tag{13}$$

Considering a parasitic capacitance of about 5 pF, and since the amplifier voltage noise is about 4 nV/$\sqrt{\text{Hz}}$, the equation yields 0.012 °C, which is well below the quantization error standard deviation that amounts to 0.1 °C/$\sqrt{12} \approx 0.03$ °C.

IV. CALIBRATION

In order to obtain an accurate output, the sensor must be calibrated in a controlled temperature environment. The parameters that have to be calibrated are the number of cycles of the secondary mode $N_2(T_0)$, the nominal resonance frequencies $f_1(T_0)$ and $f_2(T_0)$ (only at the reference temperature T_0, chosen as 25 °C), as well as the temperature coefficients α_1 and α_2 over the entire target range.

Calibration was performed by inserting the MEMS and electronics inside a climatic chamber. Temperature was swept from 85 °C down to 5 °C (to avoid issues due to condens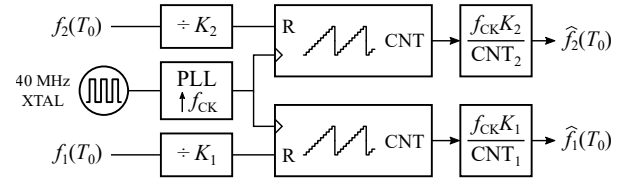ation at lower temperatures) in steps of 2.5 °C. Both the resonance frequencies and the temperature coefficients could be calibrated by acquiring the transfer function of the MEMS device in a frequency range centered on the resonant modes. Then, once N_1 is chosen, the number of cycles $N_2(T_0)$ can be simply calculated as $N_2(T_0) = \lfloor N_1 f_2(T_0)/f_1(T_0)\rfloor$.

More details are discussed in [17]. Care was taken to ensure minimal generation of heat by the board, switching off all unnecessary electronic components in this phase.

An analog temperature sensor [22] was also mounted on the board, located roughly at a 1 cm distance from the MEMS device. The information provided by the sensor was correlated to the temperature measurement provided by the chamber internal reference sensor, in order to improve the accuracy of the calibration procedure.

Note that, while the parameters at T_0 shall be calibrated for each individual sensor, the reference values for the TCfs can be derived from a family calibration only, without the need of long calibration procedure on every sample. The high repeatability of the TCf, that is the basis for such an assumption, was validated in previous works [21].

The effect of calibration errors on the output temperature can be studied starting from equation (4). Considering statistical errors on both the frequency and the TCfs, the output variance can be expressed as:

$$\sigma^2(T) = \frac{\dfrac{\sigma^2(f_{20})}{f_{20}^2} + \dfrac{\sigma^2(f_{10})}{f_{10}^2}}{(\alpha_2 - \alpha_1)^2} + \frac{\left(\dfrac{f_2(T)}{f_1(T)}\dfrac{f_{20}}{f_{10}} - 1\right)\sigma^2(\Delta\alpha)}{(\alpha_2 - \alpha_1)^4}. \tag{14}$$

In order to maintain the calibration accuracy similar to the desired ±0.05 °C resolution, the resonance frequencies at T_0 should be calibrated as accurately as:

$$\sigma(f_{1,2}) < \frac{q_{max}}{2\sqrt{12}}f_{1,2}(T_0)(\alpha_2 - \alpha_1) \approx 0.01 \text{ Hz}. \tag{15}$$

Concerning the calibration accuracy of the temperature coefficients, the error is maximum at 85 °C. In order to maintain the target accuracy, the difference between the TCfs should not vary more than:

$$\frac{\sigma(\Delta\alpha)}{\Delta\alpha} < \frac{q_{max}}{2\sqrt{12}}\frac{1 + \alpha_1\Delta T}{\Delta T} \approx 0.024\% \tag{16}$$

between samples. This is below the few 10 ppm repeatability of the TCf from part to part, found for this process in [21].

Apart from the initial calibration in the climatic chamber, which is mandatory to extract the temperature coefficients, the system also has an option of self-calibration of the frequencies and reference temperature that can be performed immediately

after turn-on, when no significant thermal gradients exist on the board, and both the MEMS and the on-board sensor are at the same temperature. A module, schematized in Fig. 6, uses an external crystal oscillator to estimate the resonance frequency by simple counting. The two frequencies are divided by K_1 and K_2, both set to 45000, and the external counting reference is raised up to 200 MHz. This enables a frequency estimate with an accuracy down to 0.01 Hz. The operation takes approximately 170 ms to acquire one frequency point.

Since the temperature computation is entirely digital, the number of bits of the system signals and calibration parameters have been chosen to enable the aforementioned calibration accuracy. Table III lists the number of bits used for the main signals and calibration parameters. The size of the other internal signals has been optimized via simulation to ensure an optimal number of bits.

V. EXPERIMENTAL RESULTS

A. Start-up and calibration validation

The first measurement aims at verifying the correct calibration, i.e. the matching between the temperature estimate provided by the MEMS-based sensor and a reference sensor. However, this is not possible in stationary conditions, as the board itself represents a heat source that generates a temperature difference between the two sensors. The chosen way to validate the calibration is, after a long thermalization with the system switched off, to analyse start-up measurements. Indeed, in the very first seconds after the system is switched on, the two sensors should yield the same value. For such test, the system is placed in an uncontrolled but isolated environment (a climatic chamber, in off state). After thermal equilibrium is reached, the electronic board is switched on and the measurements are captured. Fig. 7 shows the temperature measured by the MEMS-based sensor vs time, compared with the reference sensor. Data confirm that calibration is correct, as the initial temperature is matched within 0.1 °C. The steady-state temperature becomes larger for the MEMS-based sensor, since it is closer to the stationary heat source (i.e., the electronic components) than the reference temperature sensor.

A similar start-up procedure is then repeated to validate the calibration at another temperature point. This time the chamber is pre-heated at 80°C, allowing the temperature of all the system components to stabilize. Then the board is switched on (and simultaneously the chamber off to avoid disturbance from its controlling motors). Fig. 8 again shows how the proposed T sensor initially yields a matched temperature with the reference sensor (confirming the thermalization of the setup inside the chamber, with no other heat sources on), and then the two sensors see their temperature estimates split due to the board heating. Using the LM35 sensor to estimate the MEMS temperature would lead to a wrong value by as much as 6 °C, in agreement with what anticipated in Section II.

B. Resolution

The system is then switched on at ambient temperature and kept on for a time long enough to guarantee that the new thermal equilibrium is reached. Afterwards, Allan deviation

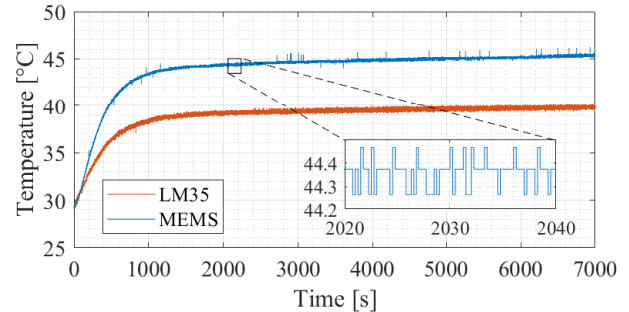| N_2	N_1	α_1, α_2	T, T_0	$M f_2(T_0)$	$f_1(T_0)$
24	18	16	14	32	26

Fig. 7. Temperature acquired by the MEMS and reference sensors at the system start-up. Due to heating of the board, the sensors start at the same temperature, then a residual offset remains in steady-state conditions. The close up shows quantization limits.

measurements are captured to validate the system resolution, and results are reported in Fig. 9. Noise is confirmed to be in the range of 30 m°C$/\sqrt{\text{Hz}}$, as expected from the former sections. A stability level is reached at about 6 m°C at an observation interval of 50 s. This, however, does not represent the ultimate limit of the sensor, but simply the limit in keeping the temperature stable within the chamber for such long times and small temperature variations. Indeed, the drift is identically visible on both the reference and the MEMS-based sensors, implying that it can be ascribed to real environmental changes and not to sensors drifts.

C. Spatial gradients

The last section analyses the effects of additional spatial gradients generated on purpose in different locations of the system, and varying in time. First, a heat source (20 W lamp) is placed close (about 1 cm) to the reference sensor (point labelled as A in Fig. 10). When the heat source is switched on, an additional difference appears between the two sensors, as the reference one is clearly closer to the
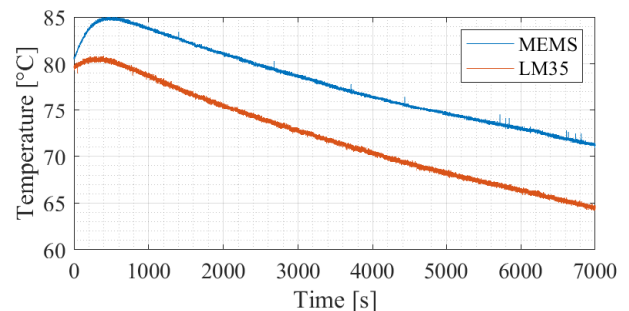

Fig. 8. System startup with pre-thermalization at 80 °C. Initially, both the MEMS and external sensor measure the same temperature; then, as the board starts heating, the measurements reach a steady state condition with a 6 °C offset.
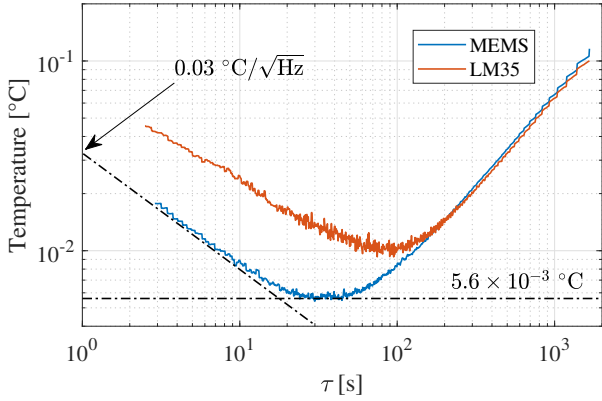
Fig. 9. Allan standard deviation of both sensors output. The digital sensor shows a bias instability of about 5.6 mK at 100 s gating intervals τ. The white noise can be extracted as 0.03 °C/$\sqrt{\text{Hz}}$ by continuation of the curve at lower τ, as the range is limited by the selected ODR.
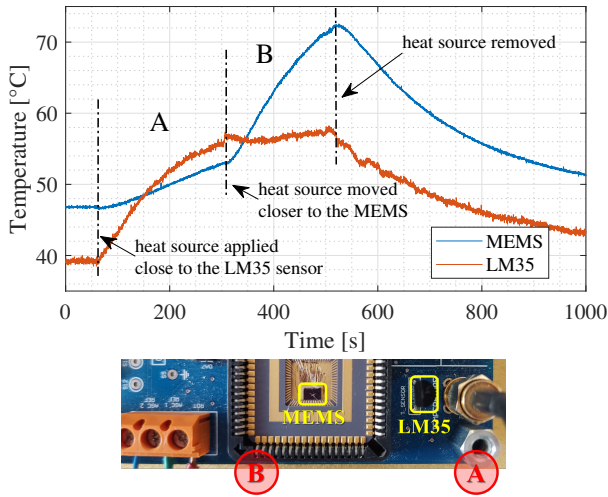

Fig. 10. Plots showing the capability of the sensor to accurately detect local temperature variations. A heat source is moved from location A to B above the test board, thus generating different heat distribution, as shown by the picture below. As the source location changes, the temperature measured by the digital sensor and the reference sensor consistently changes showing the effect of the different heat gradient.

source, and experiences a larger thermal change (Fig. 10a). As the heat source is moved closer to the MEMS-based sensor (point labelled as B in the figure), a predictable change in the temperature measured by the two sensors is seen, and the MEMS-based one now reports larger temperature values than the reference one. After the source is switched off, both sensors show the transient back to the initial values.

Once again the reported measurements confirm that, for an accurate calibration of MEMS-based sensors, a local T sensor, possibly integrated in the same die as the MEMS itself, is preferable. Huge differences between the temperature estimate by an external sensor and the MEMS itself, up to 10 °C or more, could indeed arise, deteriorating the calibration/compensation techniques that rely on real-time temperature measurements.

TABLE IV
COMPARISON WITH SIMILAR WORKS

Ref.	Resolution	ODR	Frequency	Notes
This	43 mK	4 Hz	300 kHz	Poly-Si
[12]	20 μK	100 Hz	47 MHz	TF[a] clock
[13]	30 mK[b]	N/A	200 MHz	Large $\Delta\alpha$
[14]	8 mK[b]	N/A	1-2.5 Mhz	TF clock
[16]	< 10 mK	N/A	12 MHz	Mono-Si

[a]TF: Temp-flat, i.e., temperature-stabilized reference used to measure temperature.
[b]From Allan std. dev. at 1 s averaging time.

VI. CONCLUSION

This work discussed the relevance of local temperature measurements for MEMS sensors compensation. Towards this goal, the implementation of a polysilicon-MEMS-based temperature sensor exploiting the simultaneous actuation of multiple resonant modes was discussed. The proposed architecture was implemented for the first time for a standard polysilicon process. This is indeed one key advantage, as it can be used for direct on-MEMS-chip temperature sensing for other MEMS applications, rejecting any spatial or temporal temperature gradients that may affect temperature sensors located within the ASIC or the electronic board. The sensor resolution, calculated over the maximum bandwidth of 2 Hz, i.e., half of the ODR, is proven to be 0.043 °C, with a bias stability level of about 0.0056 °C at 50 s. Concerning accuracy, for a relative temperature sensor, it depends on the initial calibration, and thus on the accuracy of the reference sensor, whose accuracy is in the order of 0.5 °C. Thus, provided that calibration is performed as described in Section IV, the estimated accuracy of our system is also in the order of 0.5 °C.

A comparison with other similar works is provided in Table IV, in terms of resolution, ODR, native resonator frequency range and notable remarks. Although at a first glance the proposed design appears to perform worse in terms of resolution than other works, it must be noted that it is compatible with a polysilicon process. It requires neither a custom process, neither a temperature-stabilized reference.

The system is currently implemented with off-the-shelf components and consumes about 500 mA current. Future works will focus on moving to a fully-integrated implementation of the oscillators and the PLLs. The total current consumption can be brought down to at least 28 mA considering [23] as reference, where similar frequency values are readout using PLLs and counters. The oscillators can be implemented as low-power Pierce circuits to cut their current consumption down to few μA [24].

REFERENCES

[1] O. Kaya, T. Köse, and K. Azgin, "Integrated temperature sensor for temperature compensation of inertial sensors," in *2019 IEEE International Symposium on Inertial Sensors and Systems (INERTIAL)*, pp. 1–2, 2019.
[2] S. Matsuda *et al.*, "Use of fluorine-doped silicon oxide for temperature compensation of radio frequency surface acoustic wave devices," *IEEE Transactions on Ultrasonics, Ferroelectrics, and Frequency Control*, vol. 59, no. 1, pp. 135–138, 2012.

[3] W.-T. Hsu, J. Clark, and C.-C. Nguyen, "Mechanically temperature-compensated flexural-mode micromechanical resonators," in *International Electron Devices Meeting 2000. Technical Digest. IEDM (Cat. No.00CH37138)*, pp. 399–402, 2000.

[4] E. J. Ng *et al.*, "Temperature dependence of the elastic constants of doped silicon," *Journal of Microelectromechanical Systems*, vol. 24, no. 3, pp. 730–741, 2015.

[5] D. D. Shin, D. B. Heinz, H.-K. Kwon, Y. Chen, and T. W. Kenny, "Lateral diffusion doping of silicon for temperature compensation of mems resonators," in *INERTIAL 2018*, pp. 1–4, 2018.

[6] A. Jaakkola *et al.*, "Determination of doping and temperature-dependent elastic constants of degenerately doped silicon from mems resonators," *IEEE Transactions on Ultrasonics, Ferroelectrics, and Frequency Control*, vol. 61, no. 7, pp. 1063–1074, 2014.

[7] A. Jaakkola, M. Prunnila, T. Pensala, J. Dekker, and P. Pekko, "Design rules for temperature compensated degenerately n-type-doped silicon mems resonators," *Journal of Microelectromechanical Systems*, vol. 24, no. 6, pp. 1832–1839, 2015.

[8] V. Zega, A. Frangi, A. Guercilena, and G. Gattere, "Analysis of frequency stability and thermoelastic effects for slotted tuning fork mems resonators," *Sensors*, vol. 18, no. 7, 2018.

[9] S. A. Gorji Zadeh, T. Saha, K. Allidina, F. Nabki, and M. N. El-Gamal, "Electronic temperature compensation of clamped-clamped beam mems resonators," in *2010 53rd IEEE International Midwest Symposium on Circuits and Systems*, pp. 1193–1196, 2010.

[10] M. Pertijs, G. Meijer, and J. Huijsing, "Precision temperature measurement using cmos substrate pnp transistors," *IEEE Sensors Journal*, vol. 4, no. 3, pp. 294–300, 2004.

[11] C.-S. Liu, R. Tabrizian, and F. Ayazi, "Temperature compensated mems oscillator using structural resistance based temperature sensing," in *2015 IEEE SENSORS*, pp. 1–4, 2015.

[12] M. Heidarpour Roshan *et al.*, "A mems-assisted temperature sensor with 20- μK resolution, conversion rate of 200 s/s, and fom of 0.04 pjk2," *IEEE Journal of Solid-State Circuits*, vol. 52, no. 1, pp. 185–197, 2017.

[13] O. Kaya, T. Köse, and K. Azgın, "A dual-resonator temperature sensing approach with time base error suppression," *IEEE Sensors Journal*, vol. 20, no. 2, pp. 707–714, 2020.

[14] C. M. Jha *et al.*, "Cmos-compatible dual-resonator mems temperature sensor with milli-degree accuracy," in *TRANSDUCERS 2007*, pp. 229–232, 2007.

[15] Y. Chen, D. D. Shin, I. B. Flader, and T. W. Kenny, "Tri-mode operation of highly doped silicon resonators for temperature compensated timing references," in *2017 IEEE 30th International Conference on Micro Electro Mechanical Systems (MEMS)*, pp. 1158–1161, 2017.

[16] M. Koskenvuori, V. Kaajakari, T. Mattila, and I. Tittonen, "Temperature measurement and compensation based on two vibrating modes of a bulk acoustic mode microresonator," in *2008 IEEE 21st International Conference on Micro Electro Mechanical Systems*, pp. 78–81, 2008.

[17] P. Frigerio, A. Fagnani, V. Zega, G. Gattere, A. Frangi, and G. Langfelder, "On-MEMS-chip Compact Temperature Sensor for Large-Volume, Low-Cost Sensor Calibration," in *MEMS 2023*, pp. 989–992, 2023.

[18] P. Frigerio, A. Fagnani, V. Zega, G. Gattere, A. Frangi, and G. Langfelder, "Compact mems temperature sensor exploiting a dual-mode polysilicon resonator and phase-locked-loop multiplication," in *TRANSDUCERS 2023)*, 2023.

[19] C. R. Marra, A. Tocchio, F. Rizzini, and G. Langfelder, "Solving fsr versus offset-drift trade-offs with three-axis time-switched fm mems accelerometer," *Journal of Microelectromechanical Systems*, vol. 27, no. 5, pp. 790–799, 2018.

[20] G. Langfelder, M. Bestetti, and M. Gadola, "Silicon mems inertial sensors evolution over a quarter century," *Journal of Micromechanics and Microengineering*, vol. 31, p. 084002, jul 2021.

[21] G. Mussi, M. Bestetti, V. Zega, A. A. Frangi, G. Gattere, and G. Langfelder, "An outlook on potentialities and limits in using epitaxial polysilicon for mems real-time clocks," *IEEE Transactions on Industrial Electronics*, vol. 67, no. 8, pp. 6996–7004, 2020.

[22] Texas Instruments, LM35 Precision Centigrade Temperature Sensors. Datasheet. [Online]. Available: https://www.ti.com.

[23] C. Padovani, M. Bestetti, C. Valzasina, A. G. Bonfanti, and G. Langfelder, "Sub-10 μhz/$\sqrt{}$hz measurement instrumentation for 140-db dr frequency-modulated mems sensors," *IEEE Transactions on Instrumentation and Measurement*, vol. 72, pp. 1–8, 2023.

[24] G. Mussi, P. Frigerio, G. Gattere, and G. Langfelder, "A mems real-time clock with single-temperature calibration and deterministic jitter cancellation," *IEEE Transactions on Ultrasonics, Ferroelectrics, and Frequency Control*, vol. 68, no. 3, pp. 880–889, 2021.